



Achieving a tunable metasurface based on a structurally reconfigurable array using SMA

XIN CHEN,^{1,2} JINSONG GAO,² AND BONAN KANG^{1,*}

¹State Key Laboratory of Integrated Optoelectronics, College of Electronic Science and Engineering, Jilin University, Changchun 130012, China

²Key Laboratory of Optical System Advance Manufacturing Technology, Changchun Institute of Optics, Fine Mechanics and Physics, Chinese Academy of Sciences, Changchun 130033, China

*kbonan@163.com

Abstract: We introduce a structurally reconfigurable metasurface which is made of shape memory alloys (SMA). It could change the morphology of the unit cells repeatedly as we expect in response to a thermal stimulus and realize a tuning range from 13.3GHz to 17.2GHz for both polarizations simultaneously. Equivalent circuit models describe the operational principle and design methodology, the physical mechanism is interpreted with the variation of surface current distribution on the structure. The experimental results coincide with the numerical simulations, making the all-metal metasurface an attractive choice for manipulating the electromagnetic wave in a wide range of spectrums with the merits of higher controllability for dynamic behavior and greater freedom for design and manufacturing.

© 2018 Optical Society of America under the terms of the [OSA Open Access Publishing Agreement](#)

OCIS codes: (160.3918) Metamaterials; (050.6624) Subwavelength structures; (260.2110) Electromagnetic optics; (260.5740) Resonance.

References and links

1. R. A. Shelby, D. R. Smith, and S. Schultz, "Experimental verification of a negative index of refraction," *Science* **292**(5514), 77–79 (2001).
2. N. Engheta and R. W. Ziolkowski, *Metamaterials: physics and engineering explorations* (Wiley-IEEE, 2006).
3. W. Cai and V. Shalaev, *Optical metamaterials: fundamentals and applications* (Springer, 2009).
4. D. R. Smith, J. B. Pendry, and M. C. Wiltshire, "Metamaterials and negative refractive index," *Science* **305**(5685), 788–792 (2004).
5. N. Yu and F. Capasso, "Flat optics with designer metasurfaces," *Nat. Mater.* **13**(2), 139–150 (2014).
6. K. Wang, J. Zhao, Q. Cheng, D. S. Dong, and T. J. Cui, "Broadband and broad-angle low-scattering metasurface based on hybrid optimization algorithm," *Sci. Rep.* **4**(1), 5935 (2014).
7. L. Liu, X. Zhang, M. Kenney, X. Su, N. Xu, C. Ouyang, Y. Shi, J. Han, W. Zhang, and S. Zhang, "Broadband metasurfaces with simultaneous control of phase and amplitude," *Adv. Mater.* **26**(29), 5031–5036 (2014).
8. L. Zhang, S. Mei, K. Huang, and C. Qiu, "Advances in full control of electromagnetic waves with metasurfaces," *Adv. Opt. Mater.* **4**(6), 818–833 (2016).
9. S. Walia, C. M. Shah, P. Gutruf, H. Nili, D. R. Chowdhury, W. Withayachumnankul, M. Bhaskaran, and S. Sriram, "Flexible metasurfaces and metamaterials: A review of materials and fabrication processes at micro- and nano-scales," *Appl. Phys. Rev.* **2**(1), 011303 (2015).
10. S. Maci, G. Minatti, M. Casaletti, and M. Bosiljevac, "Metasurfing: addressing waves on impenetrable metasurfaces," *IEEE Antennas Wirel. Propag. Lett.* **10**(1), 1499–1502 (2012).
11. C. L. Holloway, E. F. Kuester, J. A. Gordon, J. O'Hara, J. Booth, and D. R. Smith, "An overview of the theory and applications of metasurfaces: the two-dimensional equivalents of metamaterials," *IEEE Antennas Propag. Mag.* **54**(2), 10–35 (2012).
12. N. I. Zheludev and Y. S. Kivshar, "From metamaterials to metadevices," *Nat. Mater.* **11**(11), 917–924 (2012).
13. B. Zhu, K. Chen, N. Jia, L. Sun, J. M. Zhao, T. Jiang, and Y. J. Feng, "Dynamic control of electromagnetic wave propagation with the equivalent principle inspired tunable metasurface," *Sci. Rep.* **4**(1), 4971 (2014).
14. S. Liu, H. X. Xu, H. C. Zhang, and T. J. Cui, "Tunable ultrathin mantle cloak via varactor-diode-loaded metasurface," *Opt. Express* **22**(11), 13403–13417 (2014).
15. H. X. Xu, G. M. Wang, T. Cai, J. Xiao, and Y. Q. Zhuang, "Tunable Pancharatnam-Berry metasurface for dynamical and high-efficiency anomalous reflection," *Opt. Express* **24**(24), 27836–27848 (2016).
16. P. Pitchappa, C. P. Ho, P. Kropelnicki, N. Singh, D. Kwong, and C. Lee, "Micro-electro-mechanically switchable near infrared complementary metamaterial absorber," *Appl. Phys. Lett.* **104**(20), 201114 (2014).
17. Z. Su, Q. Zhao, K. Song, X. Zhao, and J. Yin, "Electrically tunable metasurface based on Mie-type dielectric resonators," *Sci. Rep.* **7**, 43026 (2017).

18. J. Chou, L. Parameswaran, B. Kimball, and M. Rothschild, "Electrically switchable diffractive waveplates with metasurface aligned liquid crystals," *Opt. Express* **24**(21), 24265–24273 (2016).
19. K. P. Chen, S. C. Ye, C. Y. Yang, Z. H. Yang, W. Lee, and M. G. Sun, "Electrically tunable transmission of gold binary-grating metasurfaces integrated with liquid crystals," *Opt. Express* **24**(15), 16815–16821 (2016).
20. H. Tao, A. C. Strikwerda, K. Fan, W. J. Padilla, X. Zhang, and R. D. Averitt, "Reconfigurable Terahertz Metamaterials," *Phys. Rev. Lett.* **103**(14), 147401 (2009).
21. I. M. Pryce, K. Aydin, Y. A. Kelaita, R. M. Briggs, and H. A. Atwater, "Highly strained compliant optical metamaterials with large frequency tunability," *Nano Lett.* **10**(10), 4222–4227 (2010).
22. J. Y. Ou, E. Plum, L. Jiang, and N. I. Zheludev, "Reconfigurable Photonic Metamaterials," *Nano Lett.* **11**(5), 2142–2144 (2011).
23. F. Ma, Y.-S. Lin, X. Zhang, and C. Lee, "Tunable multiband terahertz metamaterials using a reconfigurable electric split-ring resonator array," *Light Sci. Appl.* **3**(5), 171 (2014).
24. X. Chen, J. S. Gao, and B. N. Kang, "Achieving dynamic switchable filter based on a transmutable metasurface using SMA," *AIP Adv.* **7**(9), 095025 (2017).
25. J. M. Jani, M. Leary, A. Subic, and M. A. Gibson, "A review of shape memory alloy research, applications and opportunities," *Mater. Des.* **56**(4), 1078–1113 (2014).
26. A. Nespola, S. Besseghini, S. Pittaccio, E. Villa, and S. Viscuso, "The high potential of shape memory alloys in developing miniature mechanical devices: A review on shape memory alloy mini-actuators," *Sensor. Actuat. A-Phys.* **158**(1), 149–160 (2010).
27. G. F. Xu, N. C. Si, and Y. X. Li, "Rolling wearabilities of different structural state CuZnAl shape memory alloys," *Chin. J. Nonferrous Met.* **14**(5), 825–830 (2004).
28. Y. Bellouard, "Shape memory alloys for microsystems: A review from a material research perspective," in *Proceedings of the 7th European Symposium on Martensitic Transformations*, G. Eggeler and G. Kostorz, ed. (Elsevier, 2008), pp. 582–589.
29. M. Koyama, T. Sawaguchi, K. Ogawa, T. Kikuchi, and M. Murakami, "The effects of thermomechanical training treatment on the deformation characteristics of Fe-Mn-Si-Al alloys," *Mater. Sci. Eng. A* **497**(1–2), 353–357 (2008).
30. G. F. Xu, "The effect of transformation temperature on dry sliding wearability of CuZnAl shape memory alloys," *Res. Stud. Foundry Equip.* **23**(6), 20–23 (2001).

1. Introduction

Metamaterials are artificially engineered composites which could exhibit unique electromagnetic properties unattainable from natural materials [1–4]. As an important branch, metasurface is periodic or quasi-periodic array in an ultrathin surface which possesses the ability to fully control the propagation behavior of electromagnetic waves [5–11]. The electromagnetic response of a metasurface can be tailored by adjusting the constituent materials, sizes, shapes and arrangement of the unit cells. However, the response obtained in this way is usually fixed at the time of fabrication and the functionality cannot be dynamically modulated with versatile performances, because the production materials are essentially passive and offer no flexibility. Thus the active control of the electromagnetic response has drawn a significant attention and the research on metasurface has extended from the structural design of a determinate property to reconfigurable metasurface who has the functionality of tuning, switching or sensing [12]. These functional devices could be accomplished by integrating active components into the unit cell, such as diodes [13–15] and microelectromechanical systems (MEMS) switches [16], or by utilizing ferrite [17] and liquid crystal [18,19] as the active medium. Nevertheless, these approaches are difficult to break through the intrinsic limitations including high insertion losses, in-band fluctuations, complexity of the fabrication and lack of the design flexibility. Alternatively, structural reconfiguration is a novel and straightforward method for controlling the transmission characteristics of metasurface [20–23], unfortunately, there are also some defects in previous works involving high operating temperature, poor reversibility, small tuning range, dependence on the polarization of the incident waves or detached resonant frequencies under different polarizations. So it is still a challenge to achieve a high efficient reconfigurable metasurface with superior performance and convenience in practical application.

The work described in this paper is motivated by the need to provide an effective solution to realize a tunable metasurface without the shortcomings aforementioned and offer the theoretic support for the experiment. We design and fabricate the metasurface by employing the shape memory alloys (SMA), it has a high sensitivity to temperature that can cause

changes to the morphology of unit cells in accordance with our expectation during the suitable variation of ambient temperature. Depending on the reversible transformation between two different arrays, the all-metal metasurface could realize a wide tuning range for both polarizations simultaneously. We use the equivalent circuit models to analyze and optimize the electromagnetic behaviors of the metasurface, the experiments have been carried out to validate the design and simulations. Compared with the previous works, the proposed metasurface offers higher control over the dynamic behavior of the transformable array and enlightens the next generation of advanced electromagnetic materials with more freedom in the processes of design and manufacturing.

2. Design and optimization

For identifying the transmission characteristic of the surface easily and processing conveniently, we choose the derivative of shorted cross loop aperture element to illustrate the tuning capability through structural engineering in Ku band and propose our design methodology by equivalent circuit models whose parameter values are related to the geometrical shape of the unit cell and the polarization mode of the incoming wave.

A three-dimensional view of a shorted cross loop aperture element is shown in Fig. 1(a) including the related parameters. The equivalent circuit model of the metal element can be thought of as two separate transmission line circuits composed of several LC resonators corresponding to TE polarization (electric component lies in the Y-direction) and TM polarization (electric component lies in the X-direction) respectively as shown in Fig. 1(b) and Fig. 1(c). For TE polarization, there will be two resonant peaks in the transmission spectrum of consideration. One mainly comes from the parallel L_1 and C_1 which are derived from the narrow edges on the two flanks of the unit cell along the Y-direction and the long gaps along the X-direction in the middle respectively. L_2 and C_2 could be understood as the long stick along the Y-direction in the middle and its adjacent gaps on the top and bottom respectively, L_2 is in series with the capacitance C_2 then in parallel with capacitance C_1 to set up another resonator which brings about the second resonant peak and a null point. Analogous analysis implies that there are three peaks in the same frequency range for TM polarization, L_3 and C_3 come of the right part of the long stick along the X-direction and the long gaps along the Y-direction in the middle of the unit cell respectively while the ones on the left part represent L_4 and C_4 , C_5 originates from the short gap on the left side along the Y-direction, the narrow edges on the top and bottom along the X-direction make up L_5 .

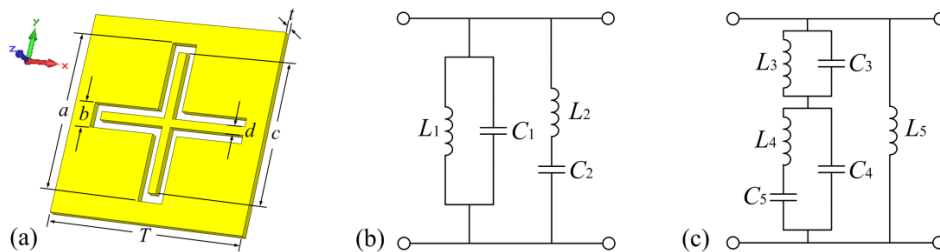


Fig. 1. (a) 3D schematic of the original unit cell, where $T = 12\text{mm}$, $a = 9.5\text{mm}$, $b = 1\text{mm}$, $c = 9\text{mm}$, $d = 0.5\text{mm}$ and $t = 0.5\text{mm}$, the impinging plane wave propagates along Z direction. The equivalent circuit models of the unit cell for (b) TE polarization and (c) TM polarization.

We construct the circuit models in the ADS circuit simulation software to calculate the S-parameters. Full-wave analysis of the structure is also performed by using CST software, in which the transmission spectrum is determined by solving the Maxwell equations in the finite-integral time-domain method, we model the structure using lossy metal whose electric conductivity is $5.8 \times 10^7 \text{ S/m}$. When the characteristic parameters of the lumped components are as follows: $C_1 = 0.625\text{pF}$, $L_1 = 0.3\text{nH}$, $C_2 = 0.226\text{pF}$, $L_2 = 0.317\text{nH}$, $C_3 = 1.305\text{pF}$, $L_3 = 0.175\text{nH}$, $C_4 = 1.448\text{pF}$, $L_4 = 0.17\text{nH}$, $C_5 = 0.4677\text{pF}$ and $L_5 = 0.4275\text{nH}$, the S-parameters of

the circuit models are consistent with the results from CST as shown in Fig. 2, which certifies the validity of the circuit models.

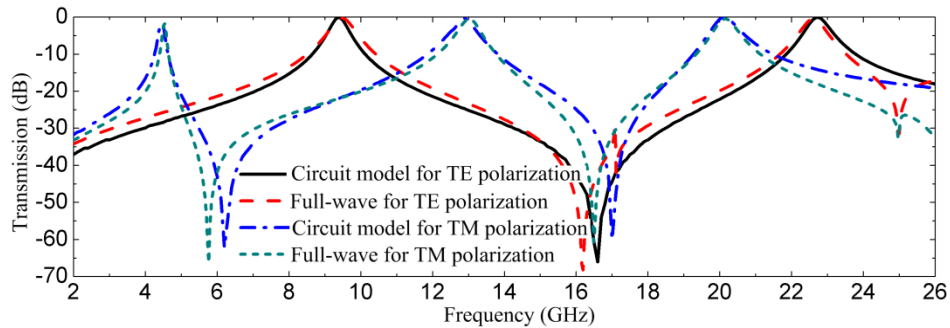


Fig. 2. Frequency response predicted by equivalent circuit models and obtained from full-wave simulations.

Thus a continuous variation of the physical configuration of the unit cell could drive dramatic alterations of inductances and capacitances, generating the new resonant status in the original frequency spectrum. One possible way to construct the pattern of tunable resonances is rotating the cross around the horizontal long stick with an angle of ω as shown in Fig. 3(a) and the variation of transmission characteristic could be understood by examining the remodeled equivalent circuits which are still similar to the prior ones except some capacitances and inductances will become adjustable if we can control the value of ω as shown in Fig. 3(b) and Fig. 3(c).

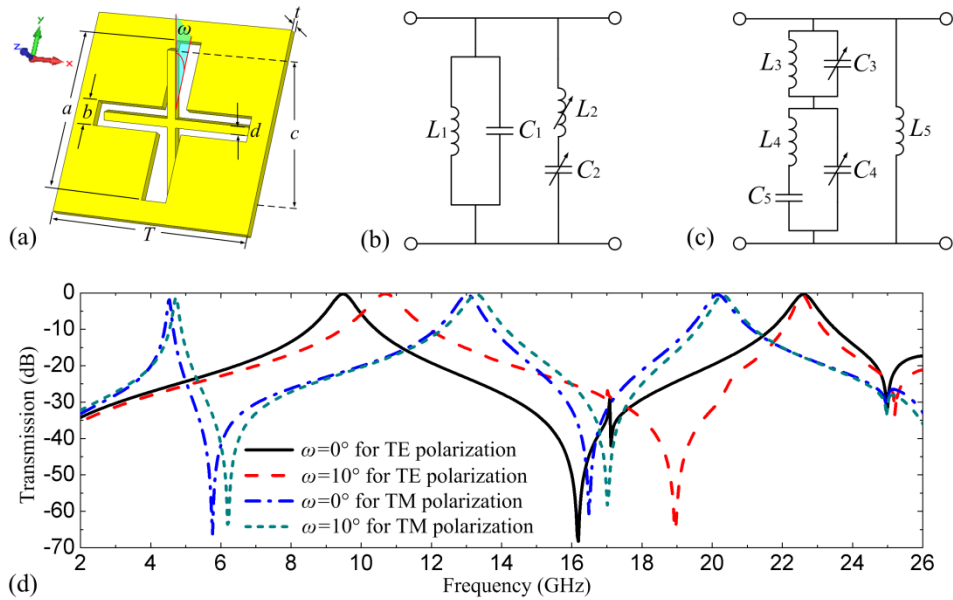


Fig. 3. (a) 3D schematic of the original unit cell with a rotating angel of ω and the corresponding equivalent circuit models for (b) TE polarization and (c) TM polarization. (d) Frequency response obtained from full-wave simulation with different values of ω for both polarizations.

When the cross rotates out of the plane for TE polarization, the effective length of the vertical long stick in the middle shortens rapidly and the gaps on its top and bottom become wider, so the reductions of L_2 and C_2 will lead to a visible shift of the null point and one resonant peak towards higher frequency; for TM polarization, the spatial extension of the

vertical long gaps in the middle brings about smaller capacitances C_3 and C_4 when the value of ω enhances, we infer that the resonant peaks and nulls can be heightened effectively owing to the decline of C_3 and C_4 , both of which are in parallel and series with different inductances. The accurate numerical simulations are performed to calculate the transmission spectrum of the metal surface under normal incidence for both polarizations. The dependence of the resonant frequencies on the value of ω is plotted in Fig. 3(d). We can find that the movements of the lower peak under TE polarization and the middle peak under TM polarization are obvious even if the cross rotates only a small angle. However, the two peaks do not locate at the same position and they possess the different sensitivity to the variation of the angle of ω due to the resonant feature of the structure.

For ensuring the availability, we properly optimize the geometric parameters of the unit cell to overlap the resonant peaks under different polarizations. The higher resonant frequency for TE polarization could be accomplished by enlarging the widths of all the vertical sticks and horizontal gaps so as to lower the values of L_1 , C_1 , L_2 and C_2 , meanwhile the variation ranges of L_2 and C_2 become smaller accordingly than before when the value of ω changes the same amount, which makes the resonant peak less sensitive to the variation of ω ; conversely, aforementioned restriction of geometrical sizes will bring about narrower gaps in the vertical direction and increase the capacitances of C_3 and C_4 , which leads to the lower resonant frequencies with a higher sensitivity to the variation of ω for TM polarization. We show the optimized design based on this idea with the modified parameters in Fig. 4 (a) where the cross has become a fat patch. A wide continuous tuning range of frequency from 13.3GHz to 17.2GHz with a negligible transmission loss is realized by changing the value of ω from 10° to 45° as shown in Fig. 4(b), additionally, the two resonant peaks under different polarizations overlap with each other all the time during moving, which becomes the peculiar fascination and novelty to distinguish this metasurface from our previous work [24], demonstrating the consequences predicted by the equivalent circuit models.

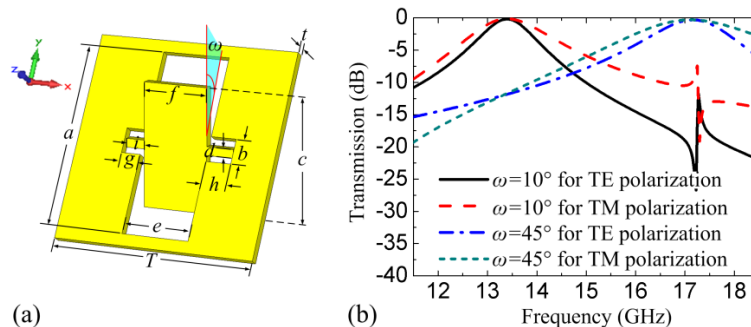


Fig. 4. (a) 3D schematic of the optimized unit cell with a rotating angle of ω , where $T = 12\text{mm}$, $a = 10.64\text{mm}$, $b = 1.44\text{mm}$, $c = 7.08\text{mm}$, $d = 0.5\text{mm}$, $e = 4\text{mm}$, $f = 3.8\text{mm}$, $g = 1.15\text{mm}$, $h = 1.5\text{mm}$, $i = 1.1\text{mm}$ and $t = 0.5\text{mm}$, the impinging plane wave propagates along Z direction. (b) Frequency response obtained from full-wave simulation with different values of ω for both polarizations.

3. Fabrication and measurement

The choice of fabrication material for the transformable array plays a critical role in the operation process, and the suitability of the material is governed by the following desired characteristics: low resistivity to maximize transmission through the surface, ability of switching between two macroscopic shapes reversibly and spontaneously, compatibility with conventional or advanced fabrication techniques. As the most qualified candidate, SMA has been characterized by the exhibition of temperature induced shape change between high-temperature phase (austenite) and low-temperature phase (martensite) repeatedly [25]. This unique functional property is acquired traditionally through a special thermomechanical

training which involves subjecting the alloy to the repeating transformation between martensite and austenite [26] after the annealing heat treatment.

The experimental alloy is prepared by induction melting of high-purity initial elements with a nominal composition of copper(69.61wt.%), zinc(25.7wt.%), aluminum(3.81wt.%), nickel(0.8wt.%), lanthanum(0.04wt.%) and cerium(0.04wt.%) under an argon atmosphere at 1250°C and homogenized at 850°C for 24h. After furnace cooling the ingot is hot-rolled and cold-rolled into a plate with the thickness of 0.5mm, then a sample of 300mm × 300mm × 0.5mm in dimension is spark cut from the plate and an array of 25 × 25 elements is realized by machining operation [27–29].

The process of annealing thermal treatment could be described as follows: the sample is heated at 850°C for 30min in vacuum followed by oil quenching at 25°C promptly, then quenched into the silicon oil at 150°C for 30min and finally quenched into the water at 50°C for 15min [30]. By this means we get the values of characteristic temperatures: $M_s = 64^\circ\text{C}$, $M_f = 52^\circ\text{C}$, $A_s = 58^\circ\text{C}$ and $A_f = 70^\circ\text{C}$, where M_s , M_f , A_s and A_f represent martensitic transformation start and finish temperature and austenitic transformation start and finish temperature respectively.

The sample is trained in rotating the fat patch of the unit cell known as “thermal training under constrain”: firstly, heating the surface higher than 70°C to the austenitic phase with electric heaters then rotate the patch of each unit cell slowly to the deformation position where the value of ω is about 60°; secondly, sustain the appearance with stress until cooling the surface below 52°C to the martensitic phase then unload the stress; finally, reheating the surface to the austenitic phase and the patch will rotate in the opposite direction spontaneously for shape recovery.

By repeating the above cycle 6 times, the surface possesses the ability to switch its morphology between two different shapes alternately without an external force on heating and cooling: when the sample is heated over 58°C, the appearance of the unit cells begin switching to the austenitic morphology by rotating the patches downwards until the temperature is higher than 70°C and then the value of ω is about 10° as shown in Fig. 5(a), the whole process takes less than five seconds and the response time highly depends on the distance between the electric heaters and the surface; after the temperature of the sample drops below 64°C, the patches set about rotating upwards to recover the martensitic morphology and finally the value of ω is about 45° at room temperature as shown in Fig. 5(b).

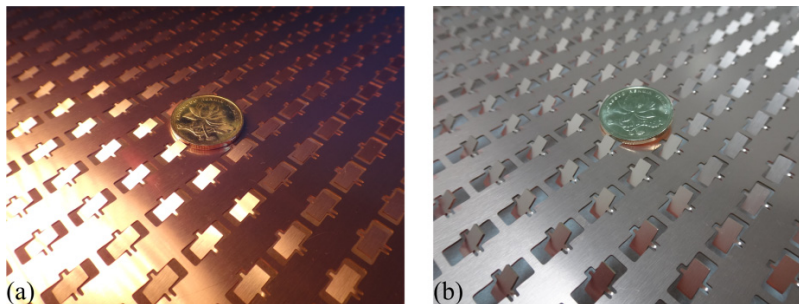


Fig. 5. The morphologies of the unit cells with external stimulations of (a) high temperature and (b) low temperature.

As shown in Fig. 6(a), we measure the tuning characteristic of the surface in a microwave anechoic chamber using a pair of horn antennas connected by a vector network analyzer, a microwave absorber with a centrally located aperture accepts the surface to minimize the measurement errors, two electric heaters are used for heating the surface to assure the temperature is high enough. The testing for both polarizations is achieved by rotating the sample 90° under normal incidence. After a cycle of heating and cooling, the resonant peaks

of different polarizations drift together from 13.3GHz to 17.2GHz with a small transmission loss of less than 0.4dB as shown in Fig. 6(b). Compared with Fig. 4(b), the curve trends of measurements and simulations are similar with each other for the same value of ω , the slight frequency deviations and expansion of the pass-band range may be ascribed to the manufacturing tolerance and the difference of rotating angle produced in the training process. Besides, as infinite arrays are simulated while finite surface is measured. However, this experiment can be used to confirm the accuracy of our prediction in the previous sections.

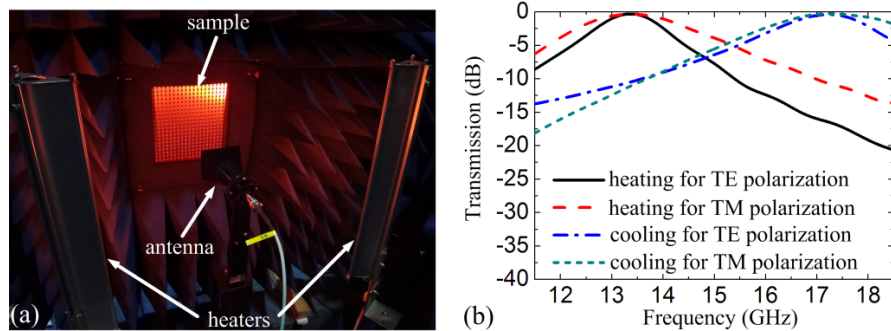


Fig. 6. (a) The experimental setup for measurement in the microwave chamber. (b) Measurement results of the sample under different temperature for both polarizations.

4. Discussion

To better understand the connection between the transformation of the unit cell structure and the drift of the resonant frequencies, we can gain some insight into the variation of maximal surface current distribution on the surface at different resonant frequencies for both polarizations as shown in Fig. 7 and Fig. 8 when the value of ω is different. The color map indicates the gradient surface current distributions and we add the arrows to represent the directions of the surface current more clearly during half cycle.

When the value of ω is 10° for TE polarization, the maximal surface current is induced around the two flank slots at 13.3GHz and flows along the metal edges in the directions of the arrows as shown in Fig. 7(a); when the value of ω is 45° , the surface current declines significantly as shown in Fig. 7(b), the reduction of the surface current will break the original resonant state and lead to an obvious descent of the transmittance at the same frequency. It predicts that we can have a major influence on the surface current distribution by changing the morphology of the unit cell. And it is indeed the case as show in Fig. 7(c) and Fig. 7(d), the surface current increases to the maximum near the same position at another resonant frequency when the inner patch structure rotates from 10° to 45° . Additionally, by comparing with Fig. 7(a), we can find that the maximal surface current flows a much shorter distance along the same routes in Fig. 7(d) where the value of ω is 45° , and the shorter flow distance is corresponding to a higher resonant frequency of 17.2GHz. That means the peak of the transmission spectrum appears with the emergence of the maximal surface current on the surface and the location of the peak depends on the distance that the maximal surface current flows through. Thus the metasurface could realize the function of tuning by transforming the morphology of the unit cell and then altering the distribution of maximal surface current on the metal structure.

For TM polarization, the electric resonances occur on the edges of the right side apertures at the corresponding resonant frequencies as shown in Fig. 8, the surface current forms two counter-circulating routes and has the same pattern of change with TE polarization when the value of ω is different, which confirms the physical mechanism of tuning described above.

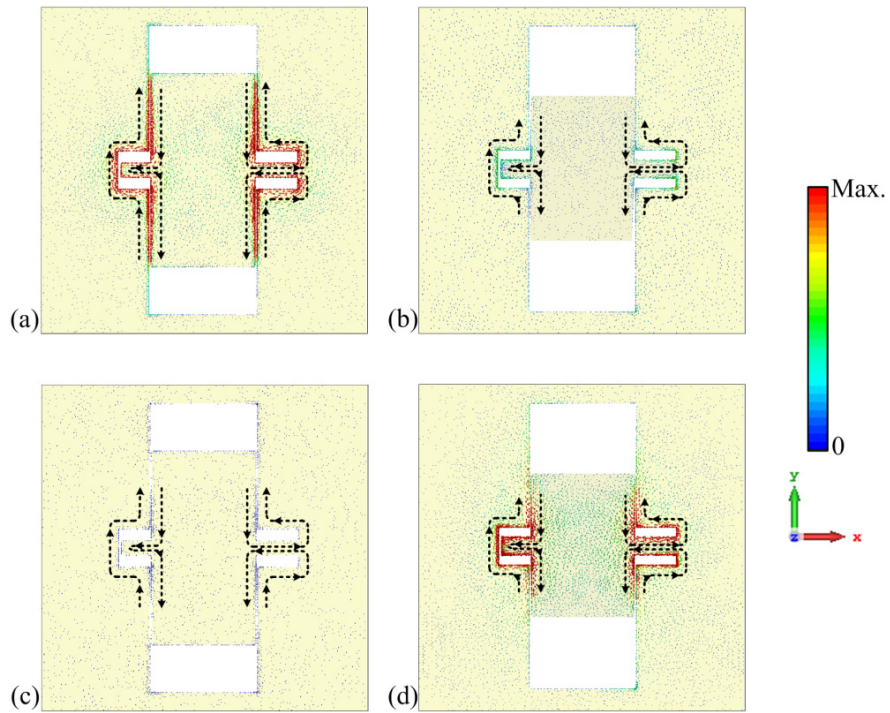


Fig. 7. Distributions of the surface currents for TE polarization under normal incidence when $\omega = 10^\circ$ (a, c) and $\omega = 45^\circ$ (b, d) at 13.3GHz (a, b) and 17.2GHz (c, d).

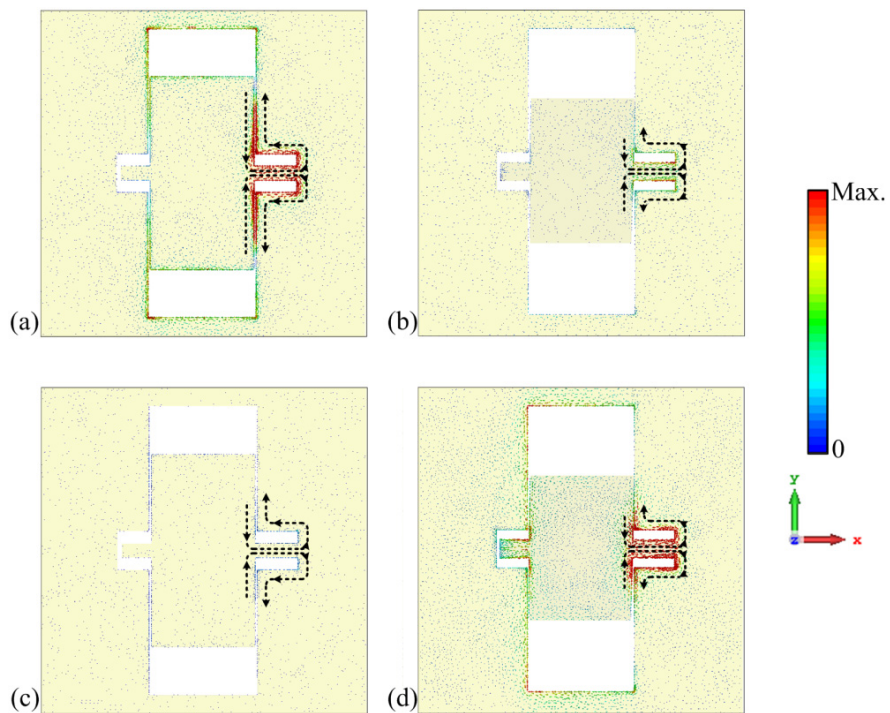


Fig. 8. Distributions of the surface currents for TM polarization under normal incidence when $\omega = 10^\circ$ (a, c) and $\omega = 45^\circ$ (b, d) at 13.3GHz (a, b) and 17.2GHz (c, d)

5. Conclusion

In summary, we provide a structurally reconfigurable metasurface for realizing metamaterial device with large-range tunable characteristic in the microwave spectrum. This is accomplished by fabricating an all-metal array of transformable unit cells which could convert the morphology between two different shapes as we expect by applying a suitable variation range of ambient temperature. We design and optimize the resonant behavior of the surface by using the equivalent circuit model and the tunability is underpinned by the full-wave simulation, the distributions of maximal surface current on different shape of metal structure are shown to have a physical insight of the mechanism. Both numeric calculations and experiment results show that the resonant peaks under different polarizations are always overlapping and can be tuned between 13.3GHz and 17.2GHz reversibly when the two different morphologies of the unit cell convert to each other. As a universal paradigm for engineering the spectral response, the all-metal metasurface can be further extended to different electromagnetic spectrums with alternative resonant structures, offering high controllability for practical applications in optical temperature sensors, tunable spectral filters, switches, modulators and any other devices where reconfiguration is required.

Funding

National Natural Science Foundation of China (NSFC) (61401424).